Unexpected concentration dependence of the mass accommodation coefficient of water on aqueous triethylene glycol droplets: Electronic Supplementary Information

Michael J. Gleichweit[1], Mercede Azizbaig Mohajer[1], Dominique P. Borgeaud dit Avocat[1], Matúš E. Divéky[1], Grégory David[1], and Ruth Signorell*[1]

[1]Department of Chemistry and Applied Biosciences, ETH Zurich, CH-8093 Zurich, Switzerland

May 23, 2024

1 Model considerations and simulation parameters

A more detailed description of the assumptions are provided in our recent article on the MHM-PA model.[1] The parameters used for the TREG-water simulations and references are listed in Table S1. For the MHM-PA part of the simulation, we chose a simulation time step of 6 ns, which corresponds to over 48'000 time steps per simulated modulation cycle. A layer thickness of $d \approx 50\,nm$ was found to be a good compromise between accuracy and numerical efficiency. Note that thinner layers did not noticeably alter the simulation results as shown in Fig. S1. Note that for thinner layers, shorter simulation time steps are required to account for the fast heat diffusion through the layers.

The assumption of a homogeneous infrared light intensity inside the droplet in the MHM-PA model is critical and thus needs to be verified. Figure S2 shows an ADDA[2] simulation of the light intensity inside an aqueous TREG droplet at 5% RH (≈0.95% water volume fraction). This represents the most extreme case of inhomogeneous light distribution inside the droplet of all experimental conditions and shows that the assumption of a homogeneous light distributions is justified.

*Corresponding author; ruth.signorell@phys.chem.ethz.ch

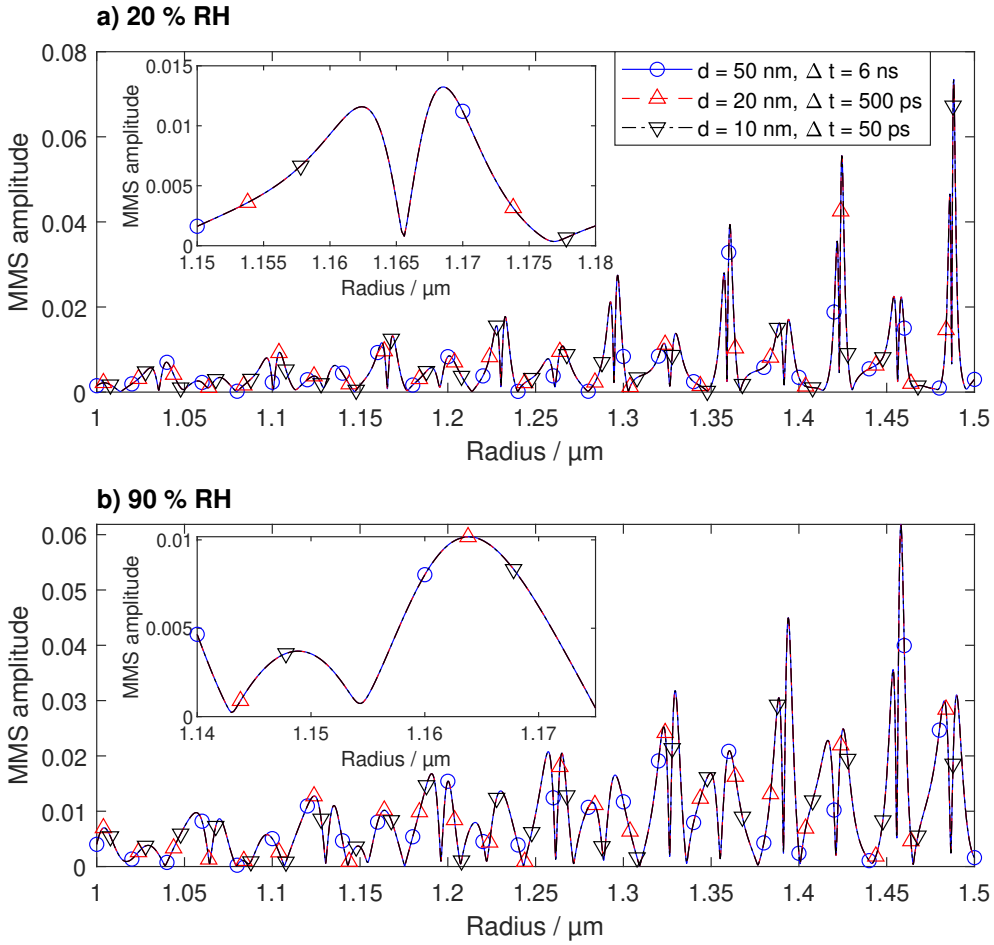

Figure S1: Simulations of the normalised MMS amplitude for (a) 20 % RH and (b) 90 % RH, for layer thicknesses of 50 nm, 20 nm and 10 nm, with according time steps of 6 ns, 500 ps and 50 ps. The different simulations differ only marginally, however, the simulation time increases drastically with number of layers and time steps. The insets show individual double-peaks in more detail.

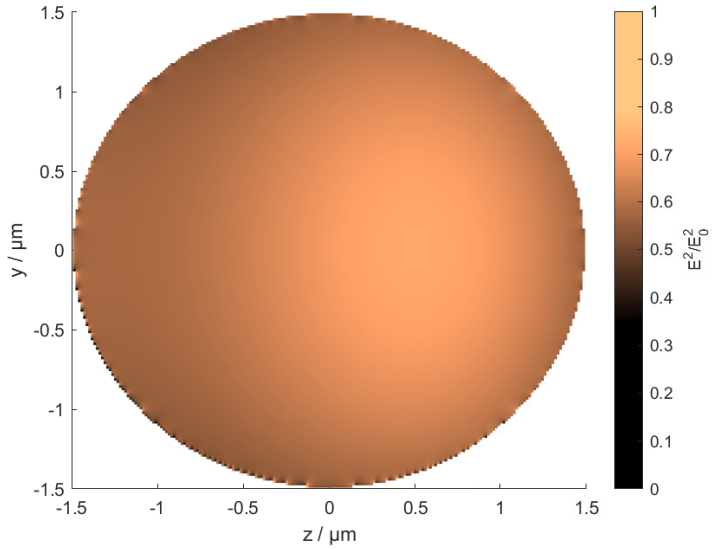

Figure S2: ADDA simulation of the infrared light intensity inside a droplet for $\lambda_{IR} = 9.456\ \mu m$, $r = 1.5\ \mu m$, $n = 1.6314 + i0.2577$ (almost pure TREG). The laser propagation direction is along the z-direction, with a Gaussian beam width $2w_0 = 148\ \mu m$. The colour bar indicates the relative light intensity inside the particle compared to the incoming light intensity.

Table S1: Simulation parameters for MHM-PA [1] and MMS simulations

Parameter	Symbol	Values	Reference
Time step	δt	6 ns	-
Layer thickness	d	46.6 - 50 nm	-
Trapping laser wavelength	λ_{trap}	532.15 nm	-
Excitation laser wavelength	λ_{IR}	9456 nm	-
Water diffusion coefficient	D_w	12 – 33 $\times$ 10^{-11} m^2 s^{-1} (RH and T dep.)	3,4
Thermal diffusivity	D_T	9.4 – 12.0 $\times$ 10^{-8} m^2 s^{-1} (RH and T dep.)	3
Specific heat capacity	C_p	2140 – 4181 J kg^{-1} K^{-1} (RH and T dep.)	3,5
Specific heat capacity of nitrogen	C_{p,N_2}	1040 J kg^{-1} K^{-1}	5
Modulation frequency	f_{mod}	3540 Hz	-
Thermal conductivity (N_2)	K	0.02597 W m^{-1} K^{-1}	5
Thermal accommodation coefficient	α_T	0.97	6
Density of aq. TREG	ρ	0.998 – 1.124 g cm^{-3} (RH and T dep.)	3,5
Mass accommodation coefficient	α_M	10^{-4} - 1	-
Latent heat	L	2450 kJ kg^{-1}	5
Refractive index TREG ($\lambda = 9456$ nm)	$n^{IR}_{TREG} + ik^{IR}_{TREG}$	1.644 + i 0.261	7, PNNL[a]
Refractive index TREG ($\lambda = 532.15$ nm)	$n_{TREG} + ik_{TREG}$	(1.4500 - 1.4466) + i 2.48·10^{-8} (T dep.)	3 7, PNNL[a]
Refractive index water ($\lambda = 9456$ nm)	$n_w + ik_w$	1.2448 + i 0.043888	8
Refractive index water ($\lambda = 532.15$ nm)	$n^{IR}_w + ik^{IR}_w$	(1.3349 - 1.3359) + i 1.4992·10^{-9} (T dep.)	9
Partial vapour pressure of H_2O	P_w	250 – 3200 Pa (RH and T dep.)	10
Objective opening angle[b]	Φ_{TTAOS}	24.49°	-
Angular resolution	$\delta\Phi$	0.5°	-

[a] Refractive index data kindly supplied by Dr. Tanya L. Myers, Pacific Northwest National Laboratory, Richland, WA, U.S.A.; [b] The objective is sightly de-focussed, which results in a higher working distance and smaller collection angle compared to collimated operation;

1.1 Data reproducibility

Figure S3 shows experimental MMS data for nine different droplets at similar relative humidities of 30-32 % recorded on two different days, which were 20 days apart. Generally, the reproducibility is very good. Small shifts in the radius (inset of Fig. S3) arise from the uncertainty of the size fitting. For droplets with radii above 1200 nm, the reproducibility of MMS signal amplitude is typically within a couple of percent. For smaller particles, the signal-to-noise ratio increases due to the low overall scattering intensity, which reduces the reproducibility usually to about 10 %.

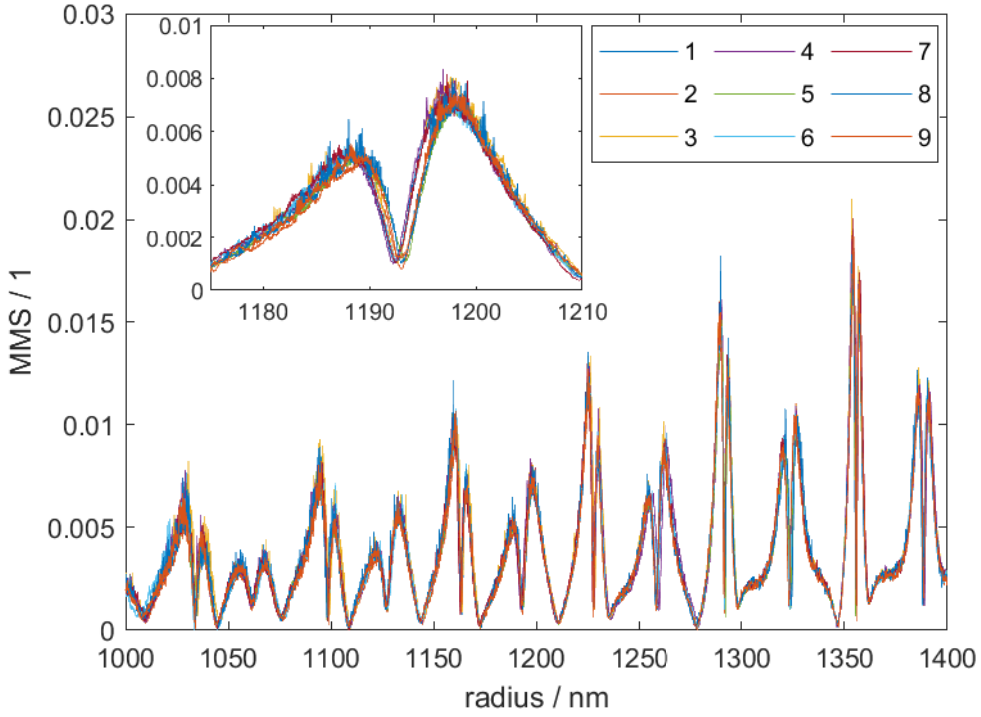

Figure S3: Comparison between several experimental MMS amplitude measurements at 30-32 % relative humidity, measured on two days, which were 20 days apart. The repeatability of MMS measurements typically lies within a couple of percent and rises to 10 % for particles smaller than ≈1200 nm.

1.2 Mass accommodation coefficient retrieval and uncertainty

The MMS simulations were performed in the RH-range of 5 % to 95 % RH in steps of 5 % RH, for 58 logarithmically spaced α_M values ranging from $10^{-4} - 1$, and with a radius resolution of 0.2 nm. With this resolution in RH and radius and a cubic spline interpolation, all experimentally relevant conditions in the measurement cell can be covered very accurately.

α_M was retrieved by a fitting method that we refer to as "full-feature fitting". In this procedure, the shape of the entire experimental MMS double-peak feature (Fig. S3 inset) is fitted to the associated feature in the simulated MMS data by minimising the normalised sum of square residuals *SSR* according to Eq. S1.

The assumption is that the individual double-peak feature is very narrow in radius (Fig. S3 inset), such that α_M does not change significantly within that range.

$$SSR = \frac{\sum \left(MMS_A^{sim,norm} - MMS_A^{exp,norm} \right)^2}{\sum MMS_A^{exp,norm}} \tag{S1}$$

Calculating Eq. S1 for α_M values over the interval $10^{-4} - 1$ results in a curve, where the minimum indicates the best estimate of α_M.

To provide meaningful uncertainties for α_M, we determined intervals of α_M values that result in simulations that were compatible with the measurement data. This sensitivity analysis considers

systematic and random error. The uncertainty in radius of the retrieved α_M-values is set by the radius range of the individual double-peak feature (Fig. S3 inset), which is much larger than the size fitting uncertainties.[11] Radius and temperature are inherently related in our system, which translates the uncertainty in radius directly to the uncertainty in temperature.[12]

2 Kinetics of mass accommodation

The main article discusses mass transfer in the transition (Knudsen) regime, where the average mean free path of gas molecules and the radius of the particles are approximately of the same order of magnitude. According to the two-step model from ref. 13, mass accommodation can be described as:

$$[\mathrm{H_2O}]_\mathrm{g} \underset{k_{des}}{\overset{k_{ads}}{\rightleftarrows}} [\mathrm{H_2O}]_\mathrm{s} \xrightarrow{k_{sol}} [\mathrm{H_2O}]_\ell \tag{S2}$$

The subscripts g indicate gas phase water molecules, s surface adsorbed molecules and ℓ liquid phase molecules. k_{ads}, k_{des} and k_{sol} describe the rate constants for adsorption, desorption and solvation, respectively. Assuming that the collision rate of gas phase water molecules with the surface is equal to the adsorption rate, the mass accommodation coefficient is

$$\alpha_M = \frac{k_{sol}[\mathrm{H_2O}]_\mathrm{s}}{k_{ads}[\mathrm{H_2O}]_\mathrm{g}} \tag{S3}$$

Assuming quasi-stationarity for surface adsorbed molecules

$$\frac{[\mathrm{H_2O}]_\mathrm{s}}{dt} = k_{ads}[\mathrm{H_2O}]_\mathrm{g} - k_{des}[\mathrm{H_2O}]_\mathrm{s} - k_{sol}[\mathrm{H_2O}]_\mathrm{s} \approx 0 \tag{S4}$$

results in:

$$[\mathrm{H_2O}]_\mathrm{g} = \frac{k_{des} + k_{sol}}{k_{ads}}[\mathrm{H_2O}]_\mathrm{s} \tag{S5}$$

From eqs. S3 and S5 we obtain

$$\frac{\alpha_M}{1-\alpha_M} = \frac{k_{sol}}{k_{des}} \tag{S6}$$

This can be expressed as a function of the Gibbs energy of the transition state ΔG_{obs} between gas phase and solvated water molecules (Fig. S4)

$$\frac{\alpha_M}{1-\alpha_M} = \exp\left(-\frac{\Delta G_{obs}}{RT}\right) \tag{S7}$$

which is related to the activation enthalpy ΔH_{obs} and the activation entropy ΔS_{obs} as follows:

$$\ln\left(\frac{\alpha_M}{1-\alpha_M}\right) = -\frac{\Delta H_{obs}}{R}\frac{1}{T} + \frac{\Delta S_{obs}}{R} \tag{S8}$$

2.1 Critical Cluster Model approach for solvation

Davidovits and coworkers suggested a nucleation model for the solvation, where newly surface adsorbed molecules form critical clusters with nearby molecules at the droplet surface, which contain $n^{\neq}$ molecules.[13,14] Figure S1 shows the Gibbs free energy diagram of the solvation process. The number of molecules in a cluster n is used here as the reaction coordinate.

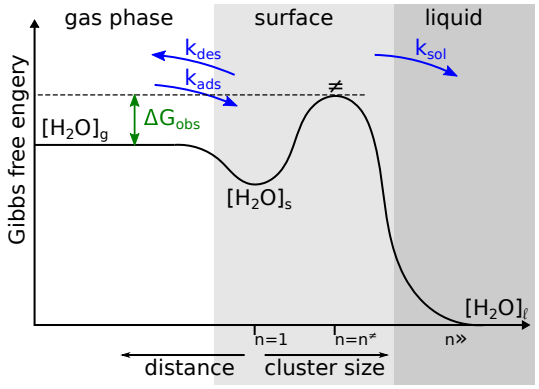

Figure S4: Gibbs energy diagram for water solvation on a particle surface. Subscripts g indicate gas phase water molecules, s surface adsorbed molecules and ℓ liquid phase molecules. $\neq$ denotes the transition state. The Figure concept was taken from Ref. 14 and re-interpreted for this publication.

References

[1] P. Corral Arroyo, M. J. Gleichweit, M. E. Diveky and R. Signorell, *Aerosol Sci. Technol.*, 2023, **57**, 742–757.

[2] M. A. Yurkin and A. G. Hoekstra, *J. Quant. Spectrosc. Radiat. Transf.*, 2011, **112**, 2234–2247.

[3] The Dow Chemical Company, *Triethylene Glycol*, Dow techreport XXX-0207X CRCG, 2007.

[4] L. Paduano, R. Sartorio, G. D'Errico and V. Vitagliano, *J. Chem. Soc., Faraday Trans.*, 1998, **94**, 2571–2576.

[5] J. Rumble, *CRC Handbook of Chemistry and Physics*, CRC Press/Taylor & Francis Group, 99th edn, 2018.

[6] P. M. Winkler, A. Vrtala, R. Rudolf, P. E. Wagner, I. Riipinen, T. Vesala, K. E. J. Lehtinen, Y. Viisanen and M. Kulmala, *J. Geophys. Res.*, 2006, **111**, D19202.

[7] T. L. Myers, T. J. Baker, O. Primera-Pedrozo, R. G. Tonkyn and T. J. Johnson, Optica Sensing Congress 2023 (AIS, FTS, HISE, Sensors, ES), 2023, p. EM3E.4.

[8] G. M. Hale and M. R. Querry, *Appl. Opt.*, 1973, **12**, 555–563.

[9] A. N. Bashkatov and E. A. Genina, Saratov Fall Meeting 2002: Optical Technologies in Biophysics and Medicine IV, 2003, pp. 393 – 395.

[10] N. A. Lange, *Langeś Handbook of Chemistry*, McGraw-Hill Education, New York, Seventeenth Edition edn, 2017.

[11] G. David, O. Reich, M. E. Divéky, S. Roy, E. A. Parmentier, J. W. Cremer, K. Esat and R. Signorell, Proc. SPIE11083, OTOM XVI, 2019, p. 1108322.

[12] M. E. Diveky, S. Roy, J. W. Cremer, G. David and R. Signorell, *Phys. Chem. Chem. Phys.*, 2019, **21**, 4721–4731.

[13] P. Davidovits, J. T. Jayne, S. X. Duan, D. R. Worsnop, M. S. Zahniser and C. E. Kolb, *J. Phys. Chem.*, 1991, **95**, 6337–6340.

[14] G. M. Nathanson, P. Davidovits, D. R. Worsnop and C. E. Kolb, *J. Phys. Chem.*, 1996, **100**, 13007–13020.